Check for updates

Sequential multistep process for fabricating reinforced membranes and electrodes using a symmetric multinozzle spray system for durable fuel cells

Yeonghwan Jang [a] , Yeonjae Lee [a], Sanghyeok Lee [a], Sungjun Kim [c], Sang Moon Kim [b,*] , Segeun Jang [a,**]

[a] School of Mechanical Engineering, Kookmin University, Seoul, 02707, Republic of Korea
[b] Department of Mechanical Engineering, Incheon National University, Incheon, 22012, Republic of Korea
[c] Hydrogen Energy Research Center, Korea Research Institute of Chemical Technology (KRICT), Daejeon, 34114, Republic of Korea

HIGHLIGHTS

- A symmetrical multi-nozzle spray enables one-step membrane-to-electrode fabrication.
- Integrated spray–heating system enables continuous fabrication without handling.
- 15 μm RCM shows 108 % higher toughness than Nafion 211, comparable to Nafion XL.
- RCM lost 6.1 % in peak power density after OCV cycling, while Nafion 211 lost 49.2 %.
- RCM shows higher initial performance and similar durability compared to Nafion XL.

GRAPHICAL ABSTRACT
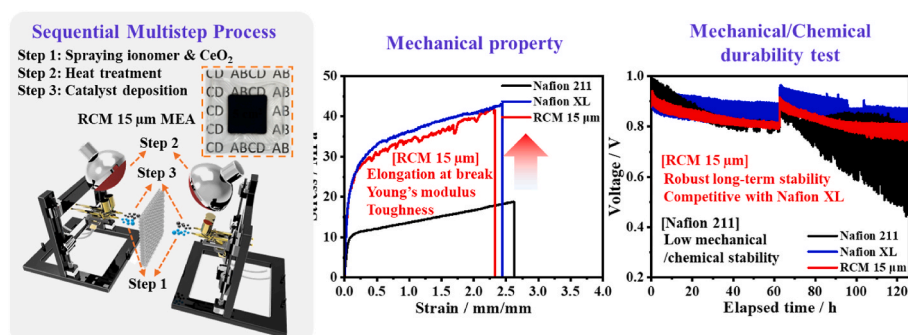
ARTICLE INFO

ABSTRACT

This study introduces a symmetric multinozzle spray–heating system for continuous membrane–electrode assembly (MEA) fabrication. The system uses symmetric nozzles and infrared heating to form a reinforced composite membrane (RCM) by impregnating a porous polytetrafluoroethylene sheet with Nafion ionomer. Simultaneously, a cerium oxide layer is applied to the anode side to enhance chemical durability, followed by sequential deposition of anode and cathode catalyst layers using another set of symmetric nozzles, thereby reducing processing time. The resulting 15-μm thick RCM exhibits 120 % and 165 % improvements in ultimate tensile strength and Young's modulus, respectively, over Nafion 211, and is comparable to Nafion XL. Durability tests under open-circuit voltage wet/dry cycling show that the MEA with the fabricated RCM maintains stable performance, with only a 6.1 % decrease in peak power density (PPD) and a hydrogen crossover current density (HCCD) of 2.34 mA/cm^2 after 6000 cycles. In comparison, Nafion 211 exhibited a 49.2 % PPD loss and an HCCD of 210 mA/cm^2, while Nafion XL showed a 19.4 % PPD loss and an HCCD of 1.62 mA/cm^2. While delivering higher initial power output, the RCM exhibited long-term durability comparable to Nafion XL, attributed to a selectively applied cerium oxide layer and a robust, well-impregnated thin membrane.

* Corresponding author.
** Corresponding author.
E-mail addresses: ksm7852@inu.ac.kr (S.M. Kim), sjang@kookmin.ac.kr (S. Jang).

1. Introduction

Recent regulations targeting carbon dioxide emissions have heightened the demand for renewable energy, with hydrogen emerging as a sustainable alternative to fossil fuels. Hydrogen fuel cells for electricity generation are utilized in various applications, including heavy-duty vehicles, drones, urban air mobility, and stationary power generation. Among the renewable power sources, polymer electrolyte membrane fuel cells (PEMFCs) are particularly favored in the transportation industry owing to their fast response characteristics, low operating temperature, and high efficiency. Despite notable technological advances and ongoing research in PEMFCs, the durability and cost of PEMFCs remain problematic [1,2]. The cost of PEMFCs is mainly contributed by the catalyst, electrolyte membrane, gas diffusion layer (GDL), and separator [1,3]. The catalyst and electrolyte membrane are the key materials of the membrane–electrode assembly (MEA), which crucially determines the system performance and durability. To minimize the catalyst usage in MEAs, researchers have developed high-activity catalysts containing ultralow Pt levels [4,5] and electrodes with low Pt loading [6–8]. In addition, fluorine-based electrolyte membranes rely on perfluorosulfonic acid (PFSA), which is manufactured by a complex process that raises the cost. Hydrocarbon-based membranes have been explored as a more economical alternative [9]. Hydrocarbon-based electrolyte membranes offer several advantages: a simple fabrication process, low raw material cost, low gas permeability, thermal stability, and environmental friendliness [9–11], but their low mechanical stability (especially under wet/dry conditions) and lower performance than PFSA-based membranes [2,12] require further research. The fabrication process of MEAs also notably contributes to the overall cost of PEMFCs [13]. The typical membrane fabrication and electrode coating techniques are casting [14,15], bar-coating [16,17], spraying [17–20], and ink-jetting [19,21]. The spray process can precisely control the thickness and uniformity of the membrane while enabling fast production through rapid solvent evaporation. Moreover, the membrane–electrode interface can be improved during the electrode deposition to obtain electrodes with high electrochemical performance [22,23]. The representative process, direct deposition of proton exchange membranes onto catalyst-coated GDL, minimizes the interfacial membrane–electrode resistance because the electrolyte membrane closely follows the roughness of the catalyst layer with high fidelity. This method also allows precise control over the membrane thickness [23, 24]. However, as the sizes of the membrane and GDL exactly match, a subgasket and precise handling are required to mitigate the risk of gas leakage. Moreover, any pinholes formed during the fabrication process can lead to gas crossover and process failure. The conventional single spray method for membrane and electrode fabrication also requires separate depositions of electrolyte solution and catalyst on the anode and cathode, respectively, along with additional heat treatment. This process is complex, time-consuming, and costly [25,26], demanding extensive space and equipment. Consequently, the production efficiency is low and novel MEA fabrication technologies are required to reduce the complexity, time, and cost of processing.

Recently, in the field of eco-friendly mobility, significant advancements have been reported in PEMFCs design optimization, hydrogen refueling infrastructure, and energy management systems. However, high costs and low durability remain major barriers to the commercialization of PEMFCs and are identified as critical challenges that must be addressed [27]. PEMFCs are prone to mechanical failure under temperature and humidity fluctuations [28–30] and chemical degradation by radicals [31,32]. During operation, PEMFCs generate water that hydrates the membrane, enhancing the ionic conductivity [33]. However, when operation ceases, the water content reduces and the membrane shrinks. Such repetitive swelling and shrinking of the electrolyte membrane can lead to mechanical fatigue, thinning of the membrane, and eventual breakdown [34,35]. Meanwhile, the main chains of the membrane are attacked and chemically degraded by reactive oxygen species (ROS) such as hydroxyl (OH•) and hydroperoxyl (OOH•) radicals generated during the PEMFCs operation [32]. These radicals form through hydrogen crossover, incomplete chemical reactions, or Fenton reactions with transition metal ions such as Fe, Cu, and Co [36–39]. Such mechanical and chemical degradation of the membrane increases the gas permeability, leading to mixed potentials, explosion risks from mixed H_2 and O_2, reduced ionic conductivity, and ultimately failure of PEMFCs. Reinforcing a composite membrane with porous polymeric substrates (e.g., expanded poly (tetrafluoroethylene) (ePTFE), polyimide, or polyethylene) can improve the mechanical stability of PEMCFs [40–42]. In the representative process, a porous ePTFE substrate is incorporated into the center of the electrolyte membrane. The chemical stability can be improved by incorporating radical scavengers with easy redox conversion, such as ceria (CeO_2) [39,43]. However, as ePTFE has low surface energy and is incompatible with the ionomer responsible for proton-transport, it cannot fully impregnate the pores during fabrication. Furthermore, CeO_2 can block ion transport, so it must be uniformly dispersed with the ionomer during the coating process. Preventing CeO_2 agglomeration remains a challenging task. To address interfacial issues, Dong et al. [44] introduced a polyphenolamine-treated ePTFE/ZrO_2 structure forming a 3D hydrogen-bond network with PFSA, improving impregnation, oxidation resistance, and overall durability. Commercial products of reinforced composite membrane (RCM) include Gore-Select and Nafion XL. Especially Nafion XL, which contains ∼ 6.0 $\mu g_{Ce}/cm^2$ ion-exchanged Ce, provides good mechanical and chemical durability. However, as it is manufactured using cast method, it has poor impregnation due to the high viscosity of the solution, and the central placement of ePTFE and selective introduction of functional particles is difficult [45,46].

We have developed a mirror-like symmetric multinozzle spray and heating system that integrates the entire process of RCM fabrication and electrode deposition. The symmetrically placed spray creates a co-spot in the ePTFE substrate to enhance the ionomer impregnation. As the solution is sprayed simultaneously from both sides, the fabrication time is half that of the conventional process. The two jet sprays are sprayed simultaneously toward a single spot on the ePTFE surface, where they collide to generate a high momentum that effectively impregnates the ionomer ink into the ePTFE substrate. This momentum is then redirected laterally, allowing the effective spreading and wicking of the ionomer, which then fills the ePTFE without defects or voids. To optimize the RCM fabrication with the symmetric multinozzle spray system, we varied the spray travel path and the distance between the spray nozzle and ePTFE substrate and analyzed the characteristics of the resulting membranes. The chemical durability and performance were maintained by incorporating a 1.125-μm thick functionalized CeO_2 thin layer on the anode side. In addition, the system is equipped with a symmetrically configured infrared thermal irradiator that operates alongside the spray, enabling rapid, immediate and simultaneous heat treatment on both sides. The PFSA ionomer deposition is followed by a thermal treatment that evaporates the residual solvent and crystallizes the RCM within a specific time. The electrolyte membrane is usually moved to an oven or furnace for crystallization under heat treatment, but the proposed system applies an infrared heating lamp directly at the fabrication site, eliminating the need for intermediate handling. After heat treatment, a catalyst slurry is directly deposited on both sides of the membrane using a symmetric multinozzle spray. This step utilizes an additional spray nozzle adjacent to the membrane fabrication nozzle for uniform catalyst deposition. This sequential multistep process fabricates both the RCM and electrode in a fixed position without the need for handling. The ultimate tensile stress and Young's modulus of the fabricated RCM were 120 % and 165 % higher than Nafion 211, respectively, and showed similar mechanical properties to the commercial RCM, Nafion XL. Consequently, the fabricated RCM resisted dimensional changes during an open-circuit-voltage (OCV) holding test with wet/dry cycling. After 6000 cycles, the peak power density (PPD) was 63.8 % and 32.3 % higher than Nafion 211 and Nafion XL, respectively. Furthermore, the

embedded CeO$_2$ layer effectively scavenged ROS, reducing the fluoride emissions in the condensed water by approximately 50 and 3 times at the anode and 67 and 4.5 times at the cathode compared to Nafion 211 and Nafion XL during the OCV holding test with wet/dry cycling. This result demonstrates RCM's high resistance to chemical degradation.

2. Material and methods

2.1. Construction of the symmetric multinozzle spray system

The mirror-like symmetric multinozzle spray system (see Fig. 1) was constructed by renovating a commercial 3D printing machine (Ender-3, China). The air-brushes (nozzle size 0.35 mm, WK-A900, Wave Inc., Republic of Korea) were mounted on each of two commercial 3D printing machines installed with a lab-made spray holder. The 3D printing machines were placed face-to-face. The solution was inserted into each spray reservoir and sprayed symmetrically toward the same spot at the center. The spray travel path and sweeping speed of the spray nozzles are controlled by G-code, a programming language for machine control that ensures the creation of single reproducible spots by the commercial 3D printing machine. The sprayed droplets converge precisely at the target spot. Through a series of optimized steps for the membrane and electrode fabrication, the spray path moves in a serpentine pattern from top to bottom (or vice versa) at 1-mm intervals. During one cycle, the center point of the area is shifted vertically (up or down) by 0.5 mm to ensure uniform deposition of the solution and a smooth surface (Fig. S1). The sweeping speed was fixed at 60 mm/s.

2.2. Fabrication of the RCM

To prepare the 2.5 wt% Nafion solution for constructing the electrolyte membrane, Nafion ionomer (5 wt%; density: 0.921 g/ml; Sigma Aldrich, United States) was diluted with isopropyl alcohol (IPA; Samchun Chemicals, Republic of Korea) at a weight ratio of 1:1. The ePTFE (~4 µm, Gen4, Donaldson Inc., United States) was fixed on a Teflon mask with a 4 cm × 4 cm square hole and placed in the center of the symmetric multinozzle spray system. The distance between the ePTFE and spray nozzle was set to 3 cm. During the RCM fabrication, the 2.5 wt % Nafion solution was sprayed from both spray nozzles at a controlled rate of ~600 µl/min. The spray rate was selected considering the simultaneous arrival and evaporation rate of the solution. Once 85 % of the Nafion solution had been consumed, 1 wt% CeO$_2$ (<25 nm particle size, 10 wt% in H$_2$O, Sigma Aldrich, United States) (relative to the total solid Nafion weight in the RCM) was added to the anode side spray reservoir. Immediately after spraying, the RCM was continuously heat-treated at 168 °C for approximately 15 min under an infrared thermal irradiator (250 W, PHILIPS, Republic of Korea).

2.3. Preparation of the membrane–electrode assembly

To prepare the catalyst slurry, commercial Pt/C (46.9 wt%; Tanaka, Japan) was mixed with deionized (DI) water, IPA, and the Nafion ionomer. The ionomer/carbon ratio was fixed at 0.6. The catalyst slurry was uniformly dispersed in an ultrasonic bath for 30 min. Using the symmetric multinozzle spray system, the catalyst inks were sprayed onto the surfaces of the Nafion 211 membrane (25 µm, Dupont, United States), Nafion XL (27.5 µm, ~6.0 µg$_{Ce}$/cm^2, Dupont, United States), and RCM. Each membrane was mounted on a Teflon mask with a 2.23 × 2.24 cm (5 cm^2) square opening and continuously exposed to an infrared thermal irradiator to prevent its swelling during the coating process. Finally, the Nafion 211, Nafion XL, and RCM were assembled into MEAs with the same catalyst loading (0.2 mg$_{Pt}$/cm^2) on both the anode and cathode sides.

2.4. Evaluation of fuel cell performance and electrochemical characteristics

The performances of the prepared MEAs were evaluated in a single cell configuration. The MEAs were sandwiched between GDL (39BB, SGL Carbon, Germany), Teflon gaskets (240 µm), serpentine bipolar plates with width and height channel dimensions of 1 mm each, and endplates, which were layered at both sides. The single cell was tightened by eight bolts under a torque of 80 in-lb and connected to a fuel cell station (CNL Energy, Republic of Korea). The single cell was activated by fully humidified H$_2$ (300 ml/min) and air (1000 ml/min) with relative humidity (RH) of 100 % supplied to the anode and cathode, respectively, without additional backpressure, at a cell temperature of 80 °C. The polarization curve was obtained after full activation by measuring down to 0.3 V at a scan rate of 50 mA/s. The corresponding electrochemical impedance spectroscopy (EIS) spectra were measured at 0.8 V using an
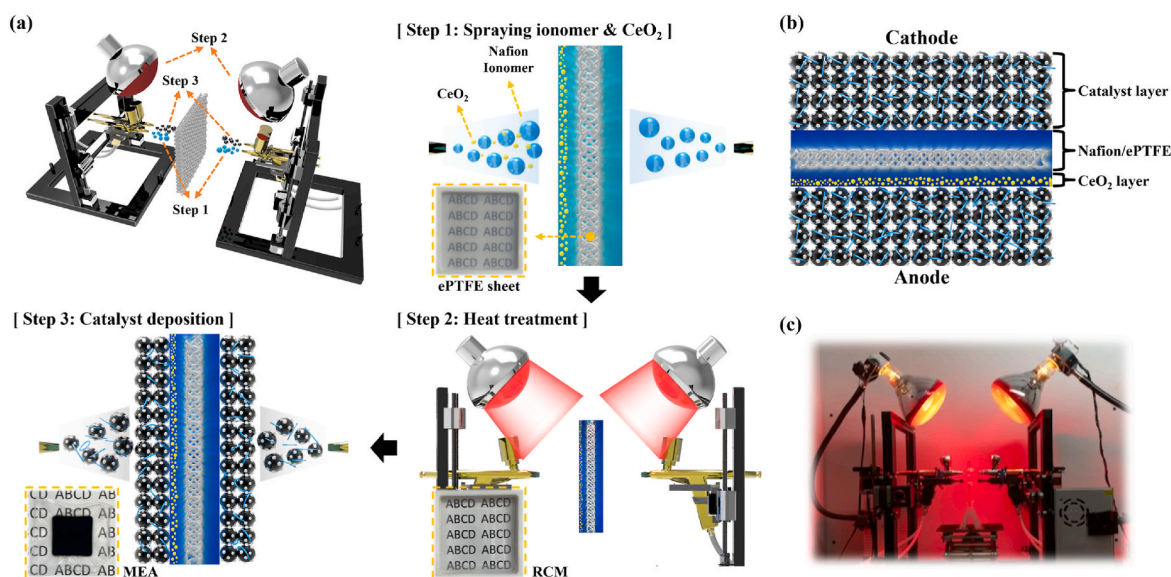

Fig. 1. (a) Schematic of the mirror-like symmetric multi-nozzle spray system, (b) Schematic of MEA configurations, and (c) Digital camera image of experiment set-up.

AC impedance analyzer (HCP-803, BioLogic, France) in the frequency range 100 kHz to 0.1 Hz with an amplitude of 10 mV. Cyclic voltammetry (CV) spectra were obtained using a potentiostat (HCP-803, Bio-Logic, France) in the 0.05–1.2 V range at a scan rate of 50 mV/s, supplying H_2 (50 ml/min) and N_2 (200 ml/min) to the anode and cathode, respectively. To compare the H_2 crossover, linear sweep voltammetry (LSV) was performed from 0.1 to 0.6 V at a scan rate of 2 mV/s.

2.5. Open-circuit-voltage holding test with wet/dry cycling

The mechanical and chemical durability of the MEAs were evaluated through an OCV holding test with wet/dry cycling as recommended by the U.S. Department of Energy (DOE). During the test, the anode and cathode were supplied with 200 ml/min H_2 and air, respectively, and the MEA was subjected to 6000 wet/dry cycles at a cell temperature of 90 °C. Each cycle consisted of 30 s at 0 % RH followed by 45 s at 100 % RH. To compare the fluoride concentrations released during the OCV holding test with wet/dry cycling, the drainage waters from the anode and cathode were collected after 3000 and 6000 cycles. Each drainage water was mixed with an equal volume of total ionic strength adjustment buffer (TISAB II, Thermo Fisher Scientific, United States) and analyzed using a calibrated fluoride-ion selective electrode coupled to a fluoride-ion meter (Orion Star A214, Thermo Fisher Scientific, United States).

2.6. Characterization methods

Surface and cross-sectional images of the membranes were captured using field emission scanning electron microscopy (FE–SEM, JSM-7610F, JEOL, Japan) and cryo-focused ion beam-scanning electron microscopy (cryo–FIB–SEM, Aquilos, Thermo Fisher Scientific, United States). The crystallinity was evaluated through X-ray diffraction (XRD, Smartlab, Rigaku, Japan) using Cu K α ($\lambda = 0.154$ nm) radiation at an accelerating voltage of 45 kV and a current of 200 mA. The 2θ range was 0°–50°. X-ray photoelectron spectroscopy (XPS, ESCALAB250, Thermo Fisher Scientific, United States) was performed over the 0–1350 eV range of binding energies with a step size of 1 eV. The stress–strain properties were measured at room temperature using an INSTRON 3340 tensiometer (Instron Corp., United States) under a head speed of 5 mm/min. Thermo-mechanical stabilities of the prepared membranes were examined by a dynamic mechanical analyzer (DMA) (Q800, TA instrument, United States) in the temperature range of 20–170 °C at a heating rate of 3 °C/min, an amplitude of 15 μm, and a frequency of 1 Hz at the Korea Research Institute of Chemical Technology (KRICT). To measure the dimensional stabilities and water uptakes of the prepared membranes, the membranes were first cut into 1 cm × 1 cm squares, then dried in a vacuum oven at 80 °C for 12 h and slowly cooled to room temperature (25 °C). The initial lengths (x_i), widths (y_i), thicknesses (z_i), and weights ((m_i) of the membranes were measured. To attain the hydrated state, the membranes were fully immersed in DI water at 80 °C for 12 h. The final lengths (x_f), widths (y_f), thicknesses (z_f), and weights (m_f) were measured after removing residual water from the membrane surfaces. The dimensional changes and water uptakes were calculated as follows:

$$Length\ change\ (\%) = \left(\frac{x_f - x_i}{x_i}\right) \times 100\% \tag{1}$$

$$Width\ change\ (\%) = \left(\frac{y_f - y_i}{y_i}\right) \times 100\% \tag{2}$$

$$Thickness\ change\ (\%) = \left(\frac{z_f - z_i}{z_i}\right) \times 100\% \tag{3}$$

$$Water\ uptake\ (\%) = \left(\frac{m_f - m_i}{m_i}\right) \times 100\% \tag{4}$$

The Proton conductivities (σ) of the membranes were calculated using the following equation:

$$\sigma = \frac{l}{R \times t \times w}\ [S\,/\,cm] \tag{5}$$

where $l, R, t,$ and w refer to the distance between the two electrodes (fixed at 1 cm), the membrane resistance (Ω), the membrane thickness (cm), and the membrane width (cm).

3. Results and discussion

Fig. 1 presents the symmetric multinozzle spray and heating system that performs the RCM fabrication, heat treatment, and electrode fabrication in a fixed position without handling. The symmetric multinozzle spray system consists of two main machines capable of biaxial movement, arranged like a decalcomania around a central porous ePTFE substrate. Each machine is equipped with multispray nozzles for ionomer and catalyst deposition and an infrared lamp for heat treatment. The RCM is fabricated through a three-step process. In Step 1, the ePTFE substrate is fixed tightly to a heat-resistant Teflon mask with a 4 cm × 4 cm square perforation and is sprayed in a serpentine pattern with 2.5 wt % Nafion solution at a flow rate of 600 μl/min, forming a co-spot. When 85 % of the total solution volume has been consumed at the anode side, the remaining 15 % of the solution is mixed with 1 wt% CeO_2 (relative to the total solid Nafion weight in the RCM). A spatially uniformly distributed CeO_2 layer with a thickness of 1.125 μm is then deposited on the anode side. To calculate the thickness of the CeO_2-distributed layer, the percentage of the CeO_2-containing solution (15 %) is multiplied by 7.5 μm, half the total thickness of the RCM (15 μm). The ePTFE porosity (85 % ± 7 %) is ignored in the calculations. The CeO_2 layer scavenges the radicals that would otherwise decompose the PTFE backbone and the side chain of the membrane. Step 2, enacted immediately after complete consumption of the Nafion solution, is the heat treatment of the RCM under an infrared thermal irradiator at 168 °C for 15 min. Heat treatment is crucial for improving the ion conductivity, crystallinity, and mechanical properties of the RCM [47–49]. During the final step, a 2.23 × 2.24 cm (5 cm^2) perforated Teflon mask is placed and the catalyst slurry is simultaneously deposited on the anode and cathode at 0.2 mg_{Pt}/cm^2 through a symmetric multinozzle spray system. The MEA with a CeO_2 embedded RCM (Fig. 1(b)) is continuously fabricated from membrane-to-electrode in a static position with no intermediate handling.

To fabricate homogeneous RCMs, the process parameters (spray travel path and nozzle-to-ePTFE substrate distance) were optimized considering the impregnation and volatilization properties of the 2.5 wt % Nafion ionomer solution. The initial evaluation was performed on RCM deposited on one side only. Fig. 2(a–d) shows schematics, digital camera images, and SEM images of an RCM coated on one side with 2.5 wt% Nafion ionomer solution. Although the ePTFE substrate was only 4 μm thick, the 2.5 wt% Nafion solution was incompletely impregnated. Therefore, RCM fabrication requires at least two repetitions of the conventional spraying method, doubling the fabrication time from that of the proposed symmetric multinozzle spray system. **Panels e–h of** Fig. 2 illustrates the impregnation results of spraying from both sides (Fig. S2). When each spray traveled in opposite directions at the same height (Fig. 2(f)), the ionomer was properly impregnated near the center where the co-spot was formed, but was unevenly distributed at the edges, revealing the inherent white color of the ePTFE substrate. When the spray nozzles were placed at different heights, the co-spots were not formed and the impregnation was unevenly distributed across the sheet (Fig. 2(h)). Nonuniform impregnation of the Nafion ionomer reduces the ionic conductivity and increases the gas permeability of the ePTFE
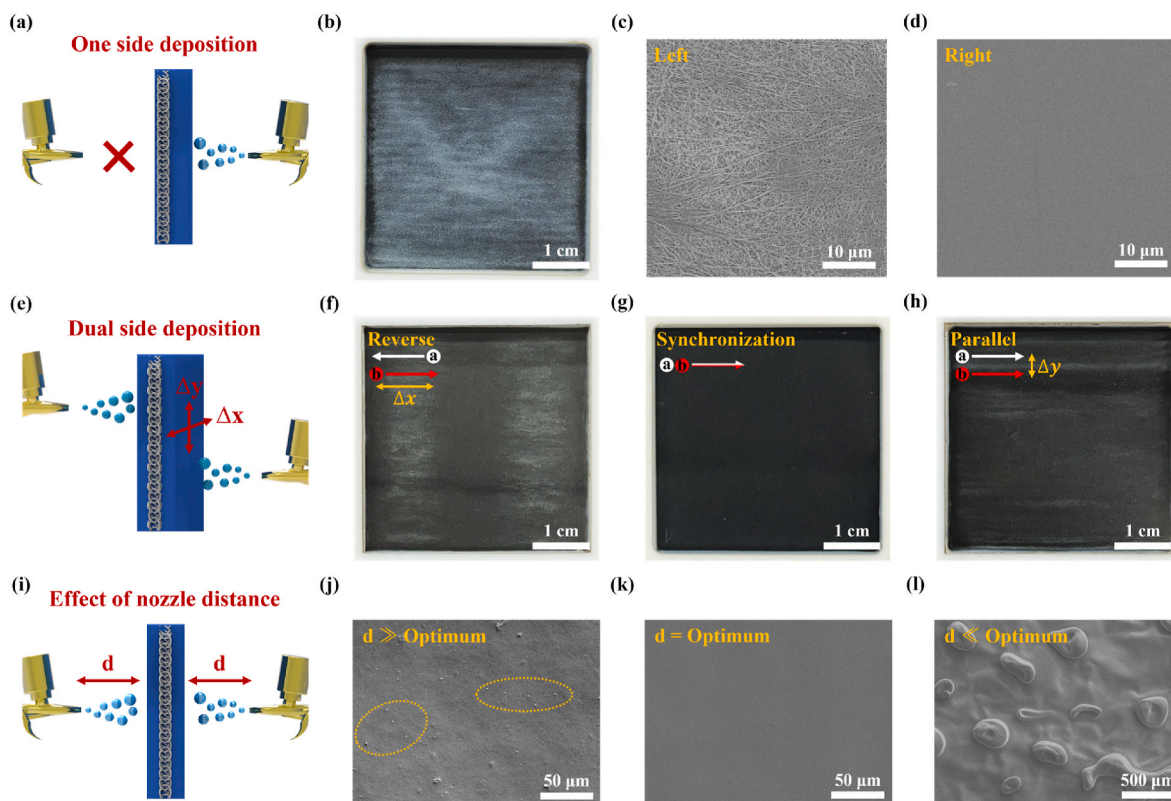
Fig. 2. (a–d) Schematic and image of RCM with ionomer applied to only right side: (b) Digital camera image, SEM images of the surface of (c) the left side and (d) the right side. (e–h) Schematic and digital camera images of various pathways for the two spray guns during deposition processes: (f) Reverse pathway, (g) synchronized pathway, and (h) parallel pathway. (i–l) Schematic and SEM image of RCM at different nozzle-to-ePTFE substrate distances: (j) Beyond the optimum distance, (k) optimum distance, (l) below the optimum distance.

substrate. In contrast, when both sprays traversed the same path to form a co-spot on the centrally located ePTFE substrate, the impregnation was highly uniform with no white lines across the surface (Fig. 2(g)). The high momentum generated by two jets colliding at a single spot was laterally redirected, enabling uniform spreading and complete filling of the ePTFE without defects or voids. Consequently, the ionomer ink was effectively impregnated into the ePTFE substrate.

To determine the optimal distance between the spray nozzle and the membrane, the ionomer impregnation and surface uniformity of an ePTFE substrate were investigated at different membrane-to-nozzle distances (Fig. 2(i–l)). When the RCM was fabricated at a distance beyond the optimal nozzle distance, the Nafion ionomer solution prematurely evaporated, forming solid Nafion particles and an uneven surface [20] (Fig. 2(j)). Conversely, when the RCM was sprayed at a shorter-than-optimal distance, the evaporation time was insufficient and large droplets containing solid Nafion formed on the surface (Fig. 2(l)). The resulting surface inhomogeneity can increase the resistance of the electrode–membrane interface. At the optimal distance, the RCM exhibited an overall uniform surface with no solid Nafion deposits (see Fig. 2(k) and subsection 2.2 for details). We also observed by cryo-FIB-SEM that the ionomer was uniformly impregnated in ePTFE over the entire area, as shown in the cross-sectional image in Fig. S3. Accordingly, the RCMs were fabricated at the optimized spray path and distance settings of the symmetric multinozzle spray system.

Fig. S4 and 3(a–c) show the XRD spectra of Nafion 211 and RCMs irradiated under the infrared thermal irradiator for varying heat treatment times. To measure the heat treatment temperature at varying distances from the infrared thermal irradiator, the Nafion 211 membrane was attached to a thermocouple. The temperatures at different distances are listed in Table S1. As the reported glass transition temperature of the Nafion ionomer ranges from 100 °C to 160 °C [50–54],

the heat treatment temperature was selected as 168 °C to ensure polymer reorganization. The XRD patterns of the Nafion 211 membrane (Fig. S4) present two broad scattering peaks at $2\theta = 10°–20°$ and $2\theta = 40°$, which are attributed to amorphous (15.5° and 40°) and crystalline (17.5°) peaks of Nafion, respectively [55,56]. Besides the broad scattering peak at $2\theta = 10°–20°$, the XRD patterns of the heat-treated RCMs display a sharp peak at $2\theta = 18°$ (Fig. 3(a–c)) attributed to the ePTFE crystalline domain of the inner ePTFE substrate [56,57]. To calculate the crystallinity, the XRD spectra were deconvoluted into peaks at 15.5° (amorphous), 17.5° (crystalline), and 18° (ePTFE crystalline domain). The crystallite size was quantified using the Debye Scherrer equation (5) [58]:

$$Crystallite\ size\ [nm] = \left(\frac{K\lambda}{\beta \cos\theta}\right) \quad (5)$$

where K is the Scherrer constant, λ is the X-ray wavelength, θ is the peak position (radians), and β is the full width at half maximum of θ (radians). The crystal size was the smallest (3.08 nm) in the untreated RCM (0 min). After 15 and 30 min of heat treatment, the crystal size increased to 3.74 and 3.85 nm, respectively, close to that of the Nafion 211 membrane (4.08 nm). As the crystal sizes of RCM 15 min and RCM 30 min differed by only 0.11 nm, we concluded that 15 min is a reasonable heat treatment time for infrared thermal irradiator considering the process efficiency. If mechanical durability is a key requirement, however, a longer heat treatment time (e.g., 30 min) may be more suitable [48].

To improve the chemical durability of the RCM, the fabrication process deposits a thin CeO_2 layer on the anode to mitigate degradation while minimizing the potential impact on oxygen reduction (ORR) reaction kinetics on the cathode side. The presence of this layer was confirmed through an XPS surface analysis. The wide spectrum (Fig. 3 (d)) displays the characteristics peaks of S 2p (~168 eV), C 1s (~289
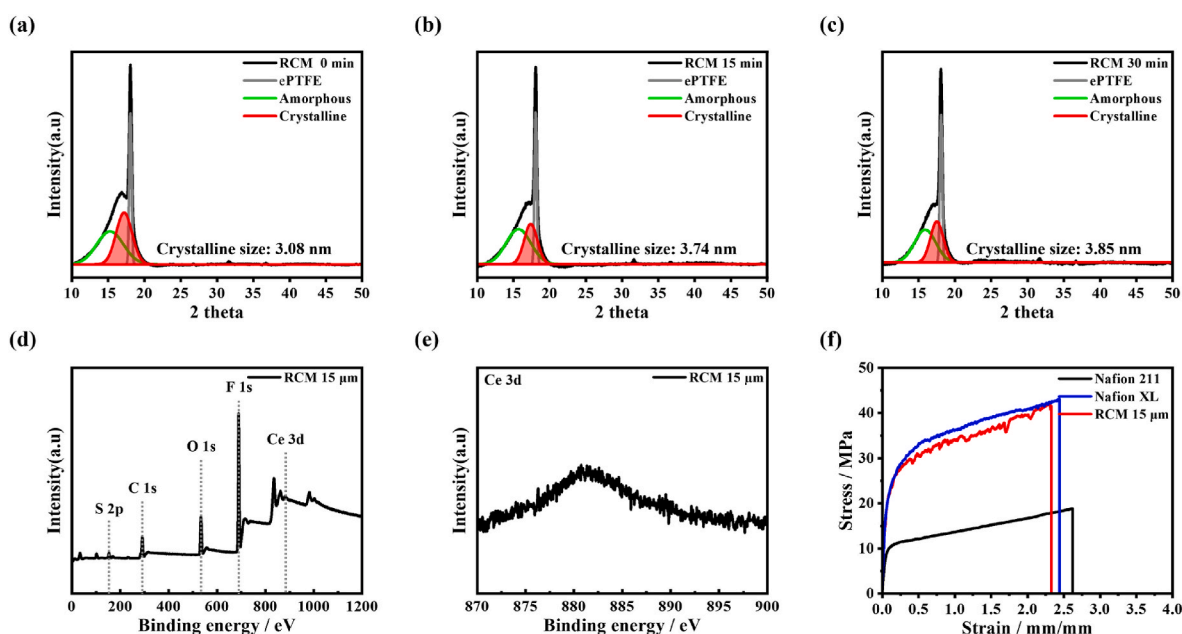
Fig. 3. XRD analysis of crystallinity variations of the RCMs depending on infrared lamp treatment time: (a) 0 min, (b) 15 min, and (c) 30 min. Characterization of CeO₂ embedded in RCM 15 μm: (d) XPS wide spectra, (e) Ce 3d spectra. (f) The measured stress-strain curves of the Nafion 211, Nafion XL, and RCM 15 μm.

eV), O 1s (~530 eV), and F 1s (687 eV), consistent with the XPS spectra of Nafion ionomer-based RCMs [59–61]. An additional peak around 882 eV (Ce 3d) (Fig. 3(e)) confirms the presence of CeO₂ [61–63]. Table 1 lists the ultimate tensile strength, Young's modulus (slopes of the linear sections), and toughness values of the Nafion 211, Nafion XL, and RCM 15 μm membranes obtained from the stress–strain curves in Fig. 3(f). Although RCM 15 μm is thinner, its ultimate tensile strength and Young's modulus exceed Nafion 211 by 120 % and 165 %, respectively. It has a similar ultimate tensile strength (−4.0 %) and Young's modulus (−7.5 %) to Nafion XL with less than 10 % difference. These improvements are attributed to the reinforcing effect of the ePTFE substrate and the well-impregnated ionomer inside the RCM. Integrating the area under the stress-strain curve, the toughness values for Nafion 211, Nafion XL, and RCM 15 μm are calculated to be 38.0, 87.9, and 78.9 MJ/m³, respectively. The toughness represents the energy absorbed by the membrane before fracture. These enhanced mechanical properties will improve the in-plane dimensional stability but might degrade the water uptake characteristics. Furthermore, the thermo-mechanical behavior was analyzed using DMA in Fig. 4. As expected, Nafion XL and RCM 15 μm with ePTFE substrate have excellent thermo-mechanical properties up to higher temperatures. On the other hand, the storage modulus of Nafion 211 shows a sharp decrease over 70 °C, suggesting a low structural stability [64]. In the tan δ curve, which is related to the glass transition temperature, it was measured to be slightly lower at RCM 15 μm due to the thin membrane thickness and in situ processing, which suggests that the membranes are relatively flexible [65]. However, the difference between Nafion 211 and Nafion XL is not significant, within about 3 °C and 4 °C, respectively. In other words, it clearly shows

that the prepared membranes have a glass transition temperature above 80 °C, suggesting that they can be sufficiently employed in the typical operating conditions of PEMFCs (60–80 °C) [66]. Consequently, the DMA analysis results confirm that the RCM 15 μm has stronger thermo-mechanical resistance compared to Nafion 211 and similar to Nafion XL. These results strongly emphasize that the symmetric multi-nozzle spray system can fabricate high-quality RCMs not only in terms of mechanical stability but also thermal stability. Furthermore, the large Young's modulus, high toughness, and stable dimensional behavior suggest that RCM 15 μm can resist mechanical breakdown under repetitive wet/dry conditions. To evaluate the impact of strong mechanical properties on water uptake by the membranes, the dimensional and weight changes of Nafion 211, Nafion XL, and RCM 15 μm were measured in completely dry and hydrated states. As the membranes are three-dimensional, their dimensional stabilities were assessed by comparing the length (x-axis), width (y-axis), and thickness (z-axis) changes between their dry and hydrated states, and their water uptakes were estimated from the weight changes. The results are summarized in Table 2. After hydration, RCM 15 μm exhibited smaller in-plane dimensions than Nafion 211 and showed similar values to Nafion XL along both the x- and y-axes, but demonstrated the greatest dimensional change along the z-axis. RCM 15 μm, which is based on a thinner ePTFE substrate (~4 μm) compared to Nafion XL (~10 μm), exhibited much higher water uptake. This resulted in higher proton conductivity than Nafion XL. The measured proton conductivities were 0.279, 0.194, and 0.256 S/cm for Nafion 211, Nafion XL, and RCM 15 μm, respectively. This trend may also be associated with differences in crystallinity, as confirmed by XRD analysis. RCM 15 μm exhibited lower crystallinity than the commercial Nafion membranes, which likely reduces the mobility inhibition of the Nafion backbone [67]. Additionally, the lower proton conductivity of Nafion XL may be attributed to the presence of non-conductive Ce distributed throughout the membrane, as well as its higher Ce loading (6.0 μg/cm²), compared to 1.4 μg/cm² for RCM 15 μm.

The in-situ electrochemical performance and durability of Nafion 211, Nafion XL, and RCM 15 μm were compared in OCV holding test with wet/dry cycling, which simultaneously evaluate the mechanical and chemical durability of the membranes (U.S. DOE) [68]. Fig. 5(a) shows the framework of the performance and durability evaluation. The

Table 1
Summary of mechanical properties of Nafion 211, Nafion XL, and RCM 15 μm.

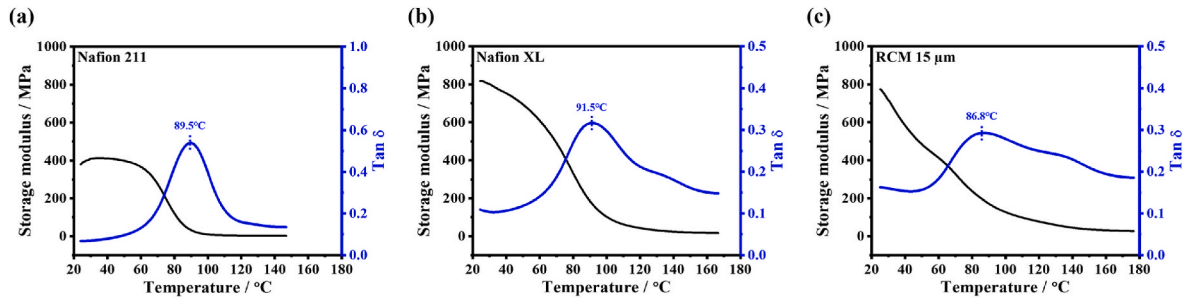|	Stress-Strain curve		
	Ultimate tensile strength [MPa]	Young's modulus [MPa]	Toughness [MJ/m³]
Nafion 211	18.8	253.6	38.0
Nafion XL	43.1	726.3	87.9
RCM 15 μm	41.4	671.7	78.9

Fig. 4. Storage modulus and tan δ curve in DMA for (a) Nafion 211, (b) Nafion XL, and (c) RCM 15 µm.

Table 2
Summary of dimensional stability, water uptake, and proton conductivity values of Nafion 211, Nafion XL, and RCM 15 µm.

	Dimensional stability			Water uptake [%]	Proton conductivity [S/cm]
	Length (x) [%]	Width (y) [%]	Thickness (z) [%]		
Nafion 211	12.5	17.5	20.8	22	0.279
Nafion XL	5.0	4.9	23.6	14.8	0.194
RCM 15 µm	5.3	5.1	33	18.5	0.256

symmetric multinozzle spray system allows easier centering of the ePTFE and easier thickness control than conventional bar-coating and casting methods for RCM fabrication [69,70]. The RCM 10 µm, RCM 15 µm, and RCM 20 µm fabricated via the symmetric multinozzle spray system all featured centrally located ePTFE substrate and well-controlled thickness (Fig. S5). The performance, EIS spectra, and hydrogen crossover current density (HCCD) of the RCMs with different thicknesses are compared in Fig. S6. RCM 10 µm exhibited a similar PPD to Nafion 211 (0.739 W/cm^2 vs. 0.774 W/cm^2) but its HCCD was more than double that of Nafion 211. Conversely, the PPD was 29.1 % lower in RCM 20 µm than in Nafion 211 (0.549 W/cm^2 vs. 0.774 W/cm^2) owing to the higher ohmic resistance and charge transfer resistance of the thicker membrane. The HCCD and PPD (0.689 W/cm^2) of RCM 15 µm
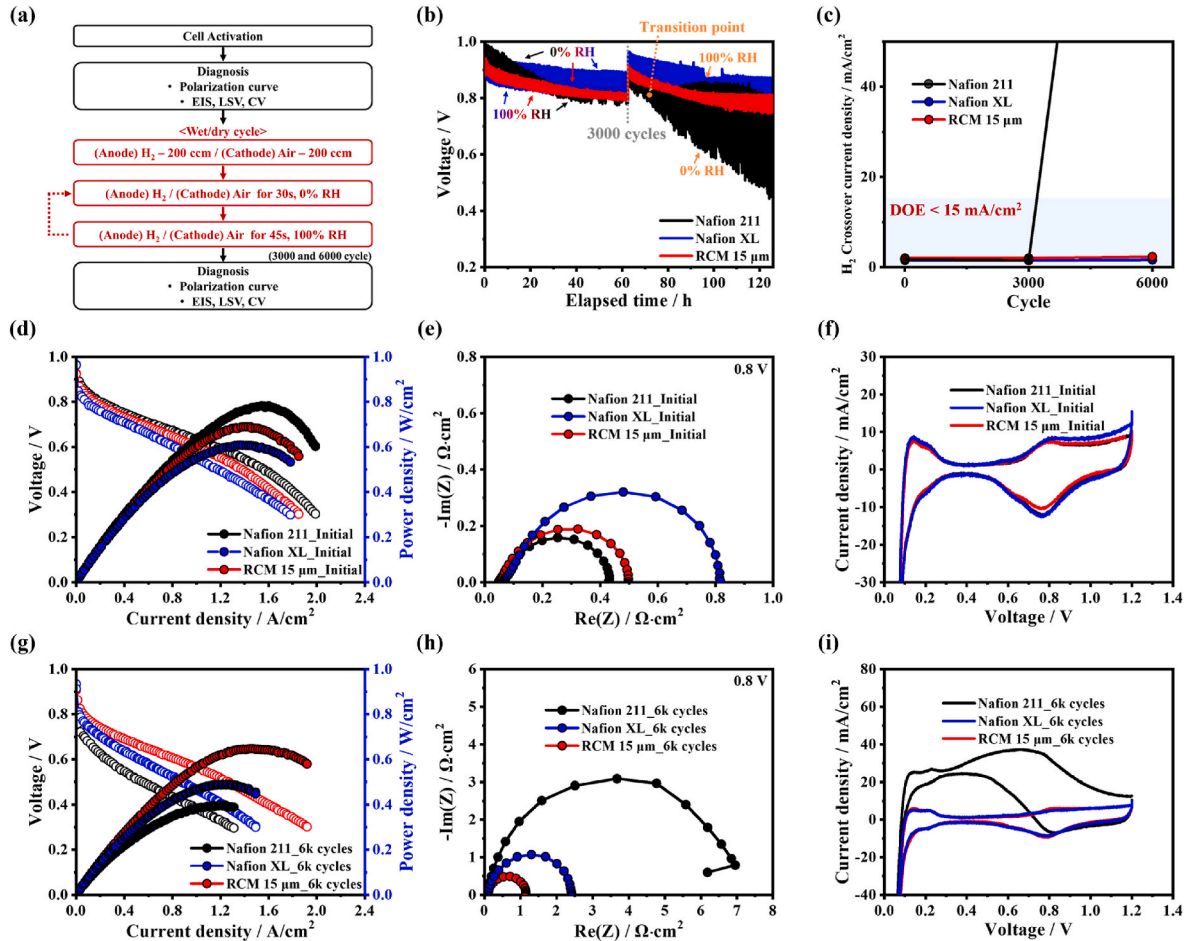

Fig. 5. (a) Flowchart of the protocol of OCV holding test combined with wet/dry cycling. (b) Plot of OCV values, (c) Plot of HCCD through LSV. (d,g) Polarization curves, (e,h) corresponding EIS spectra at 0.8 V with H$_2$/Air (150/800 ml/min), and (f,i) measurement of ECSA through CV with H$_2$/N$_2$ (50/200 ml/min) before and after OCV holding test combined with wet/dry cycling, respectively. [no back pressure, cell temperature: 80 °C (100 % RH), Pt loading: 0.2 mg$_{Pt}$/cm^2 (both side), active area: 5 cm^2].

were similar to and lower than those of Nafion 211, respectively. Considering both the performance and HCCD, 15 μm was selected as the optimal RCM thickness.

Fig. 5(b) compares the voltage behaviors of Nafion 211, Nafion XL, and RCM 15 μm during the OCV holding test with wet/dry cycling. The lower OCV in the hydrated membrane (100 % RH) than in the dry membrane (0 % RH) is attributable to hydrogen–water crossover [71, 72]. The OCV behaviors of both membranes remained stable over 3000 cycles but that of Nafion 211 reversed at 3460 cycles. Beyond this transition point (Fig. 5(b)), the OCV of the hydrated membrane declined quickly, indicating severe degradation (such as pinhole formation) at 3460 cycles. In contrast, the OCV behavior of Nafion XL and RCM 15 μm remained consistent throughout the test, with no substantial changes in HCCD (Fig. 5(c)). The HCCDs of Nafion 211, Nafion XL, and RCM 15 μm all remained stable up to 3000 cycles but that of Nafion 211 exceeded 15 mA/cm^2 at 6000 cycles. This value surpasses the U.S. DOE end-of-life target, indicating substantial degradation as evidenced in the performance, charge transfer, and electrochemical active surface area (ECSA) after the OCV holding test with wet/dry cycling. After the durability test, the PPD of Nafion 211 decreased to 0.395 W/cm^2 and the R_{LF-HF} (charge transfer resistance) @ 0.8 V increased by 1709 %. These changes were attributed to different strains in the membrane and electrode and the low dimensional stability of Nafion 211. Consequent delamination at the membrane/electrode interface and structural collapse of the electrode caused high activation losses and a large performance drop. The increased R_{LF-HF} @ 0.8 V was ascribed to the reduced proton-transport capability as the ionomer and membrane were decomposed by radicals. Nafion XL with thick initial thickness and ePTFE substrate had the lowest HCCD of 1.53 mA/cm^2 and highest OCV during the OCV holding test with wet/dry cycling. However, due to its greater thickness and distributed Ce, the initial performance was the lowest and the electrochemical degradation during the cycling test was more severe (except for HCCD) than RCM 15 μm. In contrast, the PPD and R_{LF-HF} @ 0.8 V of RCM 15 μm decreased by 6.1 % (to 0.647 W/cm^2) and increased by 144 % (to 1.096 Ω cm^2), respectively, during the OCV holding test with wet/dry cycling. The high dimensional stability of RCM 15 μm confers resistance to mechanical degradation and the CeO$_2$ layer at the anode protects the membrane and ionomer from radical attack. **Panels f and i** of Fig. 5 show the CV spectra of the MEAs before and after the OCV holding test with wet/dry cycling, respectively. The ECSAs of Nafion 211, Nafion XL, and RCM 15 μm, calculated from the hydrogen desorption peaks of the initial CV curves, were 46.9, 49.3, and 40.9 m^2/g, respectively. After 6000 cycles, the CV spectrum of Nafion 211 exhibited a gradual current increase in the forward direction, likely attributable to membrane thinning and increased hydrogen crossover caused by pinhole and crack formation. After the durability test, the ECSAs of Nafion 211, Nafion XL, and RCM 15 μm decreased by 96.2 % (to 1.8 m^2/g), 43.3 % (to 28.0 m^2/g), and 17.4 % (to 33.8 m^2/g), respectively. The severe decrease in the ECSA of Nafion 211 was caused by collapse of the electrode structure and decomposition of the ionomer by radical attack, which eliminated the three-phase boundary in the electrode. The electrochemical data of the OCV holding test with wet/dry cycling are summarized in Table 3.

To investigate the degradation of the Nafion ionomer caused by radical attacks during the OCV holding test with wet/dry cycling, the fluoride concentrations in the effluent waters were measured after 3000 and 6000 cycles. **Panels b and c** of Fig. 6 show the measured fluoride concentrations at the anode and cathode, respectively. The fluoride concentrations at both the anode and cathode of Nafion 211 sharply increased between 3000 and 6000 cycles, indicating an accelerated decomposition of the Nafion ionomer in the membrane and electrode under radical attack. In contrast, the chemical degradation of Nafion XL, RCM 15 μm was considerably suppressed by the radical scavenger layer (~6.0 μg$_{Ce}$/cm^2 of Nafion XL and ~1.4 μg$_{Ce}$/cm^2 of RCM), suggesting that even a small amount of the radical scavenger CeO$_2$ exerts a dramatic protective effect (Fig. 6(a)). In particular, RCM 15 μm exhibited the

Table 3
Summary of values of electrochemical properties before and after OCV holding test combined with wet/dry cycling.

	PPD [W/cm^2]	R_{LF-HF} @ 0.8 V [Ω•cm^2]	HCCD @ 0.4 V [mA/cm^2]	ECSA [m^2/g$_{Pt}$]
Initial				
Nafion 211	0.778	0.3817	1.70	46.9
Nafion XL	0.607	0.7522	1.53	49.3
RCM 15 μm	0.689	0.4484	2.04	40.9
6000 cycles				
Nafion 211	0.395 (−49.2 %)	6.904 (+1709 %)	210 (+12400 %)	1.8 (−96.2 %)
Nafion XL	0.489 (−19.4 %)	2.356 (−213 %)	1.62 (+1.62 %)	28.0 (−43.3 %)
RCM 15 μm	0.647 (−6.1 %)	1.096 (+144 %)	2.34 (+14.7 %)	33.8 (−17.4 %)

lowest fluoride concentration, indicating excellent radical scavenging performance by CeO$_2$ particles selectively distributed at a depth of 1.125 μm from the membrane/electrode interface on the anode side. Despite having a lower total Ce loading (1.4 μg$_{Ce}$/cm^2) than Nafion XL (6.0 μg$_{Ce}$/cm^2), RCM 15 μm demonstrated better radical scavenging effectiveness. This improvement is attributed to the strategic positioning of Ce, considering that oxygen radicals originating from H$_2$O$_2$ are predominantly formed at the anode side under OCV holding conditions [73]. Notably, the local Ce density within this targeted region was 12,366 μg$_{Ce}$/cm^3—approximately 567 % higher than that of Nafion XL (2182 μg$_{Ce}$/cm^3)—which effectively compensated for the lower overall loading and enhanced the radical scavenging efficiency. SEM images of the MEAs before and after the OCV holding test with wet/dry cycling (Fig. 6) revealed changes in the membrane thickness and surface morphology. After 6000 cycles, the thickness of the Nafion 211 MEA reduced from its initial 25 μm–14 μm and several cracks had developed on the electrode surface due to low dimensional stability and radical attack (Fig. 6(d, e, f)). In contrast, the thickness of Nafion XL and RCM 15 μm was only minimally reduced from its initial 28.0 and 15.5 μm to 27.1 and 15.1 μm, respectively (Fig. 6(g, h, j, k)). This improvement was attributed to the combined effects of the radical scavenger CeO$_2$ and the ePTFE substrate, which suppresses in-plane dimensional changes. Furthermore, as shown in Fig. 6(i–l), the absence of cracks on the electrode surfaces of Nafion XL and RCM 15 μm suggests effective reinforcement and highlights the mechanical and chemical robustness of the RCM 15 μm MEA.

These results highlight that the high durability and performance of RCM 15 μm are attributed to the symmetric multinozzle spray system, which enables the integrated fabrication of the electrolyte membrane, electrodes, and MEA as a unified process. Unlike conventional methods that require separate steps, this approach allows for simplified and efficient fabrication in a significantly shorter time, with dense ionomer impregnation, spatially controlled CeO$_2$ deposition for effective radical scavenging, and improved membrane quality through infrared heat treatment.

4. Conclusion

We presented a symmetric multinozzle spray and heating system that differs from conventional RCM fabrication process such as bar-coating, single spraying, and casting techniques. Within the symmetric system, a centrally located porous ePTFE substrate is flanked by symmetrically placed multispray nozzles and an infrared thermal irradiator in a decalcomania arrangement. The Nafion ionomer solution is sprayed from opposite spray nozzles to form a co-spot, thoroughly impregnating the ePTFE substrate and producing a high-density RCM through a
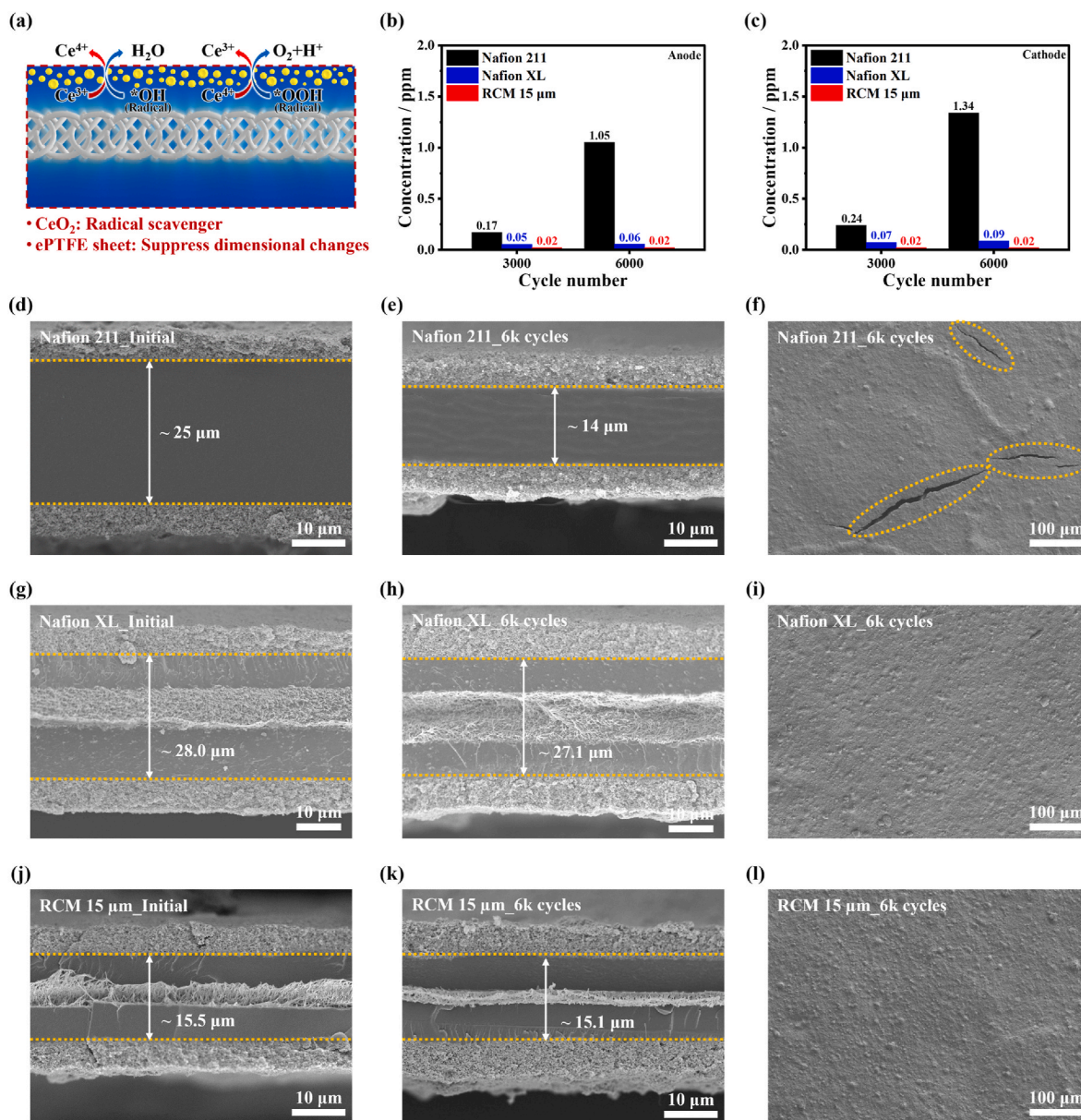
Fig. 6. (a) Schematic of radical scavenging by CeO$_2$ in RCM. Fluoride concentration in drain water for every 3000 cycles on the (b) anode and (c) cathode sides during OCV holding test combined with wet/dry cycling. Cross-sectional SEM images for prepared membranes: (d, g, j) MEAs before OCV holding test combined with wet/dry cycling and (e, h, k) the MEAs after the test. SEM images of (f) the surface of Nafion 211, (i) Nafion XL, and (l) the surface of RCM 15 μm after OCV holding test combined with wet/dry cycling.

sequential multistep process requiring no intermediate handling. Furthermore, a 1.125 μm thick layer of uniformly distributed CeO$_2$ nanoparticles (~1.4 μg/cm^2) was introduced exclusively on the anode side to enhance chemical durability while minimizing the potential impact on ORR kinetics on the cathode side. This is an extremely small amount that is 4.3 times lower than that used in the commercial RCM, Nafion XL (~6.0 μg/cm^2). After rapid heat treatment with an infrared thermal irradiator, the crystallinity level was comparable to that of Nafion 211 and the mechanical stability improved accordingly. Although thinner than the Nafion 211 membrane, RCM 15 μm demonstrated excellent dimensional stability, a large Young's modulus, and high toughness conferred by the ePTFE substrate; consequently, the RCM remained stable under repeated swelling and shrinkage. In the electrochemical analysis, Nafion 211 exhibited high initial performance but was highly susceptible to mechanical degradation, which manifested as delamination of the membrane/electrode interface and cracks in the electrode during the OCV holding test with wet/dry cycling. Nafion 211

was also vulnerable to chemical degradation, including reduction of the three-phase boundary, as the ionomers in the membrane and electrode were attacked by radicals. Nafion XL, a commercial RCM, retained OCV and HCCD effectively during cycling tests due to its thick membrane thickness (~27.5 μm), ePTFE substrate, and whole-space distributed CeO$_2$, but showed low initial performance and a significant decrease in electrochemical performance due to reduced water uptake caused by the high ePTFE/Nafion ratio (36.4 %) and high non-conductive Ce loading compared to RCM 15 μm. For RCM 15 μm with an ePTFE/Nafion ratio of 26.7 %, a significant benefit was achieved not only in dimensional stability but also in water uptake. Moreover, by selectively distributing a small amount of CeO$_2$ on the anode side, adjacent to the membrane/ electrode interface, we minimized performance drop and provided significant protection against radical attack. Our symmetric multinozzle spray system fabricates RCM with high mechanical and chemical durability as well as electrochemical performance through a simplified and efficient process, considerably reducing the production time. This

approach can potentially advance the development and commercialization of high-durability, low-cost PEMFCs.

CRediT authorship contribution statement

Declaration of competing interest

The authors declare that they have no known competing financial interests or personal relationships that could have appeared to influence the work reported in this paper.

Acknowledgment

Appendix A. Supplementary data

Supplementary data to this article can be found online at https://doi.org/10.1016/j.jpowsour.2025.237808.

Abbreviation

PEMFCs, Polymer electrolyte membrane fuel cells; RCM, Reinforced composite membrane; PPD, Peak power density; OCV, Open-circuit-voltage; GDL, Gas diffusion layer; ECSA, Electrochemical active surface area; EIS, Electrochemical impedance spectroscopy; MEA, Membrane–electrode assembly; HCCD, Hydrogen crossover current density; PFSA, Perfluorosulfonic acid; ROS, Reactive oxygen species; ePTFE, Expanded poly (tetrafluoroethylene); IPA, Isopropyl alcohol; DI, Deionized; RH, Relative humidity; CV, Cyclic voltammetry; LSV, Linear sweep voltammetry; DOE, Department of energy; FE–SEM, Field emission scanning electron microscopy; XRD, X-ray diffraction; XPS, X-ray Photoelectron Spectroscopy.

Data availability

Data will be made available on request.

References

[1] A.G. Olabi, T. Wilberforce, M.A. Abdelkareem, Energy 214 (2021) 118955, https://doi.org/10.1016/j.energy.2020.118955.

[2] D.A. Cullen, K.C. Neyerlin, R.K. Ahluwalia, R. Mukundan, K.L. More, R.L. Borup, A. Z. Weber, D.J. Myers, A. Kusoglu, Nat. Energy 6 (2021) 462–474, https://doi.org/10.1038/s41560-021-00775-z.

[3] Y. Wang, D.F. Ruiz Diaz, K.S. Chen, Z. Wang, X.C. Adroher, Mater. Today 32 (2020) 178–203, https://doi.org/10.1016/j.mattod.2019.06.005.

[4] O. Lori, L. Elbaz, ChemCatChem 12 (2020) 3434–3446, https://doi.org/10.1002/cctc.202000001.

[5] D. Chakraborty, T.E.L. Smitshuysen, A. Kakekhani, S.P.F. Jespersen, S. Banerjee, A. Krabbe, N. Hagen, H. Silva, J. Just, C.D. Damsgaard, S. Helveg, A.M. Rappe, J. K. Nørskov, I. Chorkendorff, J. Phys. Chem. C 126 (2022) 16194–16203, https://doi.org/10.1021/acs.jpcc.2c05213.

[6] L. González Rodríguez, R. Campana Prada, M. Sanchez-Molina, T.A. Rodríguez Victoria, Int. J. Hydrogen Energy 46 (2021) 17550–17561, https://doi.org/10.1016/j.ijhydene.2020.03.114.

[7] D.H. Lee, G.T. Yun, G. Doo, S. Yuk, H. Guim, Y. Kim, W. Bin Jung, H.T. Jung, H. T. Kim, Nano Lett. 22 (2022) 1174–1182, https://doi.org/10.1021/acs.nanolett.1c04354.

[8] Y. Kim, H.E. Bae, D. Lee, J. Kim, E. Lee, S. Oh, J.H. Jang, Y.H. Cho, M. Karuppannan, Y.E. Sung, T. Lim, O.J. Kwon, J. Power Sources 533 (2022) 231378, https://doi.org/10.1016/j.jpowsour.2022.231378.

[9] S. Ahmad, T. Nawaz, A. Ali, M.F. Orhan, A. Samreen, A.M. Kannan, Int. J. Hydrogen Energy 47 (2022) 19086–19131, https://doi.org/10.1016/j.ijhydene.2022.04.099.

[10] C.S. Gittleman, A. Kongkanand, D. Masten, W. Gu, Curr. Opin. Electrochem. 18 (2019) 81–89, https://doi.org/10.1016/j.coelec.2019.10.009.

[11] P.A. García-Salaberri, Sustain. Mater. Technol. 38 (2023) e00727, https://doi.org/10.1016/j.susmat.2023.e00727.

[12] M. Xu, H. Xue, Q. Wang, L. Jia, Int. J. Hydrogen Energy 46 (2021) 31727–31753, https://doi.org/10.1016/j.ijhydene.2021.07.038.

[13] B.D. James, J.M. Huya-Kouadio, C. Houchins, D.A. Desantis, Mass Production Cost Estimation of Direct H₂ PEM Fuel Cell Systems for Transportation Applications: 2018 Update, 2018. https://www.energy.gov/sites/prod/files/2019/12/f70/fcto-sa-2018-transportation-fuel-cell-cost-analysis.pdf. Accessed 28 March 2025.

[14] M. Tawalbeh, A. Al-Othman, A. Ka'ki, S. Mohamad, M. Faheem Hassan, Int. J. Hydrogen Energy 67 (2024) 852–862, https://doi.org/10.1016/j.ijhydene.2023.12.161.

[15] G. Xu, Z. Wu, Z. Wei, W. Zhang, J. Wu, Y. Li, J. Li, K. Qu, W. Cai, Renew. Energy 153 (2020) 935–939, https://doi.org/10.1016/j.renene.2020.02.056.

[16] C. Yang, N. Han, Y. Wang, X.Z. Yuan, J. Xu, H. Huang, J. Fan, H. Li, H. Wang, ACS Sustain. Chem. Eng. 8 (2020) 9803–9812, https://doi.org/10.1021/acssuschemeng.0c02386.

[17] E. Lee, D.H. Kim, C. Pak, Appl. Surf. Sci. 510 (2020) 145461, https://doi.org/10.1016/j.apsusc.2020.145461.

[18] W. Yu, X. Yang, X. Liang, Y. Xu, X. Shen, X. Ge, L. Wu, T. Xu, J. Mater. Chem. A 11 (2023) 9002–9008, https://doi.org/10.1039/d3ta00603d.

[19] B.H. Lim, E.H. Majlan, A. Tajuddin, T. Husaini, W.R. Wan Daud, N.A. Mohd Radzuan, M.A. Haque, Chin. J. Chem. Eng. 33 (2021) 1–16, https://doi.org/10.1016/j.cjche.2020.07.044.

[20] E. Choi, S.M. Kim, S. Jang, Adv. Mater. Technol. 7 (2022) 2101360, https://doi.org/10.1002/admt.201970019.

[21] A. Willert, F.Z. Tabary, T. Zubkova, P.E. Santangelo, M. Romagnoli, R.R. Baumann, Int. J. Hydrogen Energy 47 (2022) 20973–20986, https://doi.org/10.1016/j.ijhydene.2022.04.197.

[22] S. Vierrath, M. Breitwieser, M. Klingele, B. Britton, S. Holdcroft, R. Zengerle, S. Thiele, J. Power Sources 326 (2016) 170–175, https://doi.org/10.1016/j.jpowsour.2016.06.132.

[23] M. Klingele, M. Breitwieser, R. Zengerle, S. Thiele, J. Mater. Chem. A 3 (2015) 11239–11245, https://doi.org/10.1039/c5ta01341k.

[24] M. Klingele, B. Britton, M. Breitwieser, S. Vierrath, R. Zengerle, S. Holdcroft, S. Thiele, Electrochem. Commun. 70 (2016) 65–68, https://doi.org/10.1016/j.elecom.2016.06.017.

[25] E. Choi, H. Kang, Y. Jang, J.H. Kim, H.S. Ahn, S.M. Kim, S. Jang, Adv. Mater. Technol. 9 (2024) 2301191, https://doi.org/10.1002/admt.202301191.

[26] M.S. Mu'min, M. Komma, D. Abbas, M. Wagner, A. Krieger, S. Thiele, T. Böhm, J. Kerres, J. Membr. Sci. 685 (2023) 121915, https://doi.org/10.1016/j.memsci.2023.121915.

[27] T. Abedin, J. Pasupuleti, J.K.S. Paw, Y.C. Tak, M. Mahmud, M.P. Abdullah, M. Nur-E-Alam, J. Power Sources 640 (2025) 236769, https://doi.org/10.1016/j.jpowsour.2025.236769.

[28] Y. Qin, S. Ma, Y. Chang, Y. Liu, Y. Yin, J. Zhang, Z. Liu, K. Jiao, Q. Du, Int. J. Hydrogen Energy 46 (2021) 8722–8735, https://doi.org/10.1016/j.ijhydene.2020.12.043.

[29] J. Liu, Y. Yin, J. Zhang, T. Zhang, X. Zhang, H. Chen, J. Power Sources 512 (2021) 230487, https://doi.org/10.1016/j.jpowsour.2021.230487.

[30] J.P. Sabawa, A.S. Bandarenka, Int. J. Hydrogen Energy 46 (2021) 15951–15964, https://doi.org/10.1016/j.ijhydene.2021.02.088.

[31] V.D. Cong Tinh, D. Kim, J. Membr. Sci. 613 (2020) 118517, https://doi.org/10.1016/j.memsci.2020.118517.

[32] G. Li, W. Zheng, X. Li, S. Luo, D. Xing, P. Ming, B. Li, C. Zhang, Int. J. Hydrogen Energy 74 (2024) 17–30, https://doi.org/10.1016/j.ijhydene.2024.05.393.

[33] H. Eskandari, D.K. Paul, A.P. Young, K. Karan, ACS Appl. Mater. Interfaces 14 (2022) 50762–50772, https://doi.org/10.1021/acsami.2c12667.

[34] J. Chen, A. Goshtasbi, A.P. Soleymani, M. Ricketts, J. Waldecker, C. Xu, J. Yang, T. Ersal, J. Jankovic, J. Power Sources 476 (2020) 228576, https://doi.org/10.1016/j.jpowsour.2020.228576.

[35] P.M. Ngo, T. Karimata, T. Saitou, K. Ito, J. Power Sources 556 (2023) 232446, https://doi.org/10.1016/j.jpowsour.2022.232446.

[36] Y. Pang, Y. Duan, Q. Li, B. Liu, X. Hu, Q. Liu, C. Zhao, J. Membr. Sci. 686 (2023) 121999, https://doi.org/10.1016/j.memsci.2023.121999.

[37] R. Borup, J. Meyers, B. Pivovar, Y.S. Kim, R. Mukundan, N. Garland, D. Myers, M. Wilson, F. Garzon, D. Wood, P. Zelenay, K. More, K. Stroh, T. Zawodzinski, J. Boncella, J.E. McGrath, M. Inaba, K. Miyatake, M. Hori, K. Ota, Z. Ogumi, S. Miyata, A. Nishikata, Z. Siroma, Y. Uchimoto, K. Yasuda, K.I. Kimijima, N. Iwashita, Chem. Rev. 107 (2007) 3904–3951, https://doi.org/10.1021/cr050182l.

[38] A. Pozio, R.F. Silva, M. De Francesco, L. Giorgi, Electrochim. Acta 48 (2003) 1543–1549, https://doi.org/10.1016/s0013-4686(03)00026-4.

[39] Z. Tu, X. He, W. Gao, C. Zhang, H. Chen, X. Du, H. Zhang, L. Zhao, C. Wang, Z. Mao, Int. J. Hydrogen Energy 50 (2024) 41–51, https://doi.org/10.1016/j.ijhydene.2023.08.013.

[40] Y. Xing, L. Liu, Z. Li, Y. Li, Z. Fu, H. Li, Energy Fuels 36 (2022) 11177–11185, https://doi.org/10.1021/acs.energyfuels.2c01974.

[41] J.E. Cha, S. Jang, D.J. Seo, J. Hwang, M.H. Seo, Y.W. Choi, W.B. Kim, Chem. Eng. J. 454 (2023) 140091, https://doi.org/10.1016/j.cej.2022.140091.

[42] G. Cheng, Z. Li, S. Ren, D. Han, M. Xiao, S. Wang, Y. Meng, Polymers 13 (2021) 1–12, https://doi.org/10.3390/polym13040523.

[43] C. Lim, A.S. Alavijeh, M. Lauritzen, J. Kolodziej, S. Knights, E. Kjeanga, ECS Electrochem. Lett. 4 (2015) F29–F31, https://doi.org/10.1149/2.0081504eel.

[44] Y. Dong, C. Feng, H. Xie, Y. He, C.M. Costa, S. Lanceros-Méndez, J. Han, W. He, Inorg. Chem. Front. 11 (2024) 4459–4468, https://doi.org/10.1039/d4qi01074d.

[45] Y.S. Lee, H. Kim, S.M. Lee, M. Yuk, E. Kim, T.H. Kim, S.K. Kim, Appl. Surf. Sci. 671 (2024) 160728, https://doi.org/10.1016/j.apsusc.2024.

[46] L. Liu, Y. Li, R. Qiao, Y. Xing, H. Li, Energy Fuels 35 (2021) 12482–12494, https://doi.org/10.1021/acs.energyfuels.1c01205.

[47] J.E. Hensley, J.D. Way, S.F. Dec, K.D. Abney, J. Membr. Sci. 298 (2007) 190–201, https://doi.org/10.1016/j.memsci.2007.04.019.

[48] J. Li, X. Yang, H. Tang, M. Pan, J. Membr. Sci. 361 (2010) 38–42, https://doi.org/10.1016/j.memsci.2010.06.016.

[49] T.A. Pham, L.V. Nam, E. Choi, M.S. Lee, T.S. Jun, S. Jang, S.M. Kim, Energy Fuels 35 (2021) 11525–11532, https://doi.org/10.1021/acs.energyfuels.1c01225.

[50] K.Y. Cho, H.Y. Jung, K.A. Sung, W.K. Kim, S.J. Sung, J.K. Park, J.H. Choi, Y. E. Sung, J. Power Sources 159 (2006) 524–528, https://doi.org/10.1016/j.jpowsour.2005.10.106.

[51] A.V. Lyulin, S. Sengupta, A. Varughese, P. Komarov, A. Venkatnathan, ACS Appl. Polym. Mater. 2 (2020) 5058–5066, https://doi.org/10.1021/acsapm.0c00875.

[52] X. Ren, E. Gobrogge, F.L. Beyer, J. Membr. Sci. 637 (2021) 119645, https://doi.org/10.1016/j.memsci.2021.119645.

[53] G. Alberti, R. Narducci, M.L. Di Vona, S. Giancola, Fuel Cells 13 (2013) 42–47, https://doi.org/10.1002/fuce.201200126.

[54] Y.S. Kim, L. Dong, M.A. Hickner, T.E. Glass, V. Webb, J.E. McGrath, Macromolecules 36 (2003) 6281–6285, https://doi.org/10.1021/ma0301451.

[55] S. Yu, Z. Zhu, M. Zhou, H. Yu, G. Kang, Y. Cao, J. Appl. Polym. Sci. 138 (2021) 50254, https://doi.org/10.1002/app.50254.

[56] X. Teng, J. Dai, J. Su, Y. Zhu, H. Liu, Z. Song, J. Power Sources 240 (2013) 131–139, https://doi.org/10.1016/j.jpowsour.2013.03.177.

[57] Z. Zuo, Y. Yang, L. Song, Z. Zhang, X. Jin, Tribol. Lett. 69 (2021) 1–19, https://doi.org/10.1007/s11249-021-01513-y.

[58] S. Amirabadi, M. Kheradmandkeysomi, A. Zandieh, P. Serles, N. Tanguy, T. Filleter, M. Sain, C.B. Park, J. Mater. Sci. Technol. 198 (2024) 208–220, https://doi.org/10.1016/j.jmst.2024.01.081.

[59] C.Y. Yen, C.H. Lee, Y.F. Lin, H.L. Lin, Y.H. Hsiao, S.H. Liao, C.Y. Chuang, C.C. M. Ma, J. Power Sources 173 (2007) 36–44, https://doi.org/10.1016/j.jpowsour.2007.08.017.

[60] C. Chen, G. Levitin, D.W. Hess, T.F. Fuller, J. Power Sources 169 (2007) 288–295, https://doi.org/10.1016/j.jpowsour.2007.03.037.

[61] D. Zhu, W. Liu, R. Zhao, Z. Shi, X. Tan, Z. Zhang, Y. Li, L. Ji, X. Zhang, J. Mater. Sci. Technol. 109 (2022) 20–29, https://doi.org/10.1016/j.jmst.2022.02.003.

[62] J.W. Guo, T.S. Zhao, J. Prabhuram, R. Chen, C.W. Wong, J. Power Sources 156 (2006) 345–354, https://doi.org/10.1016/j.jpowsour.2005.05.093.

[63] M.A. Scibioh, S.K. Kim, E.A. Cho, T.H. Lim, S.A. Hong, H.Y. Ha, Appl. Catal., B 84 (2008) 773–782, https://doi.org/10.1016/j.apcatb.2008.06.017.

[64] L.G. Boutsika, A. Enotiadis, I. Nicotera, C. Simari, G. Charalambopoulou, E. P. Giannelis, T. Steriotis, Int. J. Hydrogen Energy 41 (2016) 22406–22414, https://doi.org/10.1016/j.ijhydene.2016.08.142.

[65] M. Peng, G. Xiao, X. Tang, Y. Zhou, Macromolecules 47 (2014) 8411–8419, https://doi.org/10.1021/ma501590x.

[66] X. Tang, Y. Zhang, S. Xu, Energy 283 (2023) 128456, https://doi.org/10.1016/j.energy.2023.128456.

[67] C. Yin, Z. Wang, Y. Luo, J. Li, Y. Zhou, X. Zhang, H. Zhang, P. Fang, C. He, J. Phys. Chem. Solid. 120 (2018) 71–78, https://doi.org/10.1016/j.jpcs.2018.04.028.

[68] T. Benjamin, R. Borup, N. Garland, C. Gittleman, B. Habizbadeh, S. Hirano, Fuel Cell Technical Team Roadmap, Off. Energy effic, Renew. Energy (2017). Accessed 1 July 2025, https://www.energy.gov/sites/prod/files/2017/11/f46/FCTT_Roadmap_Nov_2017_FINAL.pdf.

[69] C.K. Hwang, K.A. Lee, J. Lee, Y. Kim, H. Ahn, W. Hwang, B.K. Ju, J.Y. Kim, S. Y. Yeo, J. Choi, Y.E. Sung, I.D. Kim, K.R. Yoon, Nano Energy 101 (2022) 107581, https://doi.org/10.1016/j.nanoen.2022.107581.

[70] Z. Huang, B. Lv, L. Zhou, Tao wei, X. Qin, Z. Shao, J. Membr. Sci. 644 (2022) 120099, https://doi.org/10.1016/j.memsci.2021.120099.

[71] K.D. Baik, I.M. Kong, B.K. Hong, S.H. Kim, M.S. Kim, Appl. Energy 101 (2013) 560–566, https://doi.org/10.1016/j.apenergy.2012.06.034.

[72] T. Sakai, H. Takenaka, E. Torikai, J. Electrochem. Soc. 133 (1986) 88, https://doi.org/10.1149/1.2108551.

[73] S. Lee, W. Jang, M. Kim, J.E. Shin, H.B. Park, N. Jung, D. Whang, Small 15 (2019) 1903705, https://doi.org/10.1002/smll.201903705.